

## Document Version

Final published version

## Citation (APA)

Liang, Y., Bodnar, D., Mouli, G. R. C., Ragni, D., & Bauer, P. (2024). Charging Demand Prediction - Small All-Electric Aircraft and Electric Vertical Takeoff and Landing Aircraft. *IEEE Transactions on Transportation Electrification*, 11(1), 2732-2747. <https://doi.org/10.1109/TTE.2024.3427841>

## Important note

To cite this publication, please use the final published version (if applicable).  
Please check the document version above.

## Copyright

In case the licence states "Dutch Copyright Act (Article 25fa)", this publication was made available Green Open Access via the TU Delft Institutional Repository pursuant to Dutch Copyright Act (Article 25fa, the Taverne amendment). This provision does not affect copyright ownership.  
Unless copyright is transferred by contract or statute, it remains with the copyright holder.

## Sharing and reuse

Other than for strictly personal use, it is not permitted to download, forward or distribute the text or part of it, without the consent of the author(s) and/or copyright holder(s), unless the work is under an open content license such as Creative Commons.

## Takedown policy

Please contact us and provide details if you believe this document breaches copyrights.  
We will remove access to the work immediately and investigate your claim.

***Green Open Access added to TU Delft Institutional Repository***

***'You share, we take care!' - Taverne project***

**<https://www.openaccess.nl/en/you-share-we-take-care>**

Otherwise as indicated in the copyright section: the publisher is the copyright holder of this work and the author uses the Dutch legislation to make this work public.

# Charging Demand Prediction: Small All-Electric Aircraft and Electric Vertical Takeoff and Landing Aircraft

Yawen Liang<sup>1</sup>, Graduate Student Member, IEEE, Dávid Bodnár<sup>2</sup>,  
Gautham Ram Chandra Mouli<sup>3</sup>, Member, IEEE, Daniele Ragni<sup>4</sup>,  
and Pavol Bauer<sup>5</sup>, Senior Member, IEEE

**Abstract**—Electric aircraft (EA) is a promising alternative to conventional fuel-based aircraft, offering reduced greenhouse gas emissions and enhanced operational efficiency. To ensure seamless operations and optimize energy management, accurate EA charging demand prediction becomes imperative. This article presents a study on forecasting the charging demand for future small- and short-range EA. First, battery sizes are determined for various types of small all-EA (AEA) and electric vertical takeoff and landing (eVTOL) aircraft. Utilizing the electrical circuit model (ECM) for lithium-ion batteries (LIBs), this study derives the charging power curve of EA under the constant current–constant voltage (CC–CV) charging strategy. Subsequently, the charging demand prediction is conducted using the flight schedule of a selected airport, allowing for a realistic assessment of the power requirements for charging EA. Finally, case studies exploring charging demand under different scenarios are conducted. The results highlight the substantial power demand associated with the charging process, emphasizing the essential infrastructure needs and potential approaches for managing charging power in electric flight.

**Index Terms**—All-electric aircraft (AEA), charging demand prediction, constant current–constant voltage (CC–CV) charging, electric vertical takeoff and landing (eVTOL) aircraft, electrical circuit model (ECM).

## I. INTRODUCTION

OVER the last decades, the growth in fossil fuel consumption and the resulting carbon emission have underscored the shift toward electrification in the global aviation industry. The growing imperative to mitigate greenhouse gas emissions has accelerated the adoption of electric aircraft (EA), driven by their significant environmental advantages and quieter

operations compared with the traditional aircraft powered by fossil fuels. Moreover, the aerodynamic efficiency during flight is improved. In small aircraft, the internal combustion engines typically achieve an efficiency level of approximately 25%, whereas electric motors demonstrate notably higher efficiency, ranging between 90% and 95%. Consequently, the overall system efficiency of a fully battery-powered aircraft can be as elevated as 73%. Hence, the operational costs are reduced through a total energy consumption reduction [1], [2], [3]. Among various aircraft types, small all-EA (AEA) and electric vertical takeoff and landing (eVTOL) aircraft with limited range are anticipated to be a particularly viable option for aircraft electrification in the coming decade, given the ongoing advancements in the battery technology [4]. However, the successful integration of AEA and eVTOL into existing aviation infrastructure necessitates accurate estimation of battery size for both AEA and eVTOL, given the limited available information. Subsequently, the corresponding charging demand needs to be evaluated based on flight schedules, which allows for effective energy and infrastructure capacity planning at the airports to support the charging requirements. The detailed workflow for charging demand prediction is illustrated in Fig. 1. To predict the charging demand  $P_{ch}$ , key parameters include charging duration  $T_{ch}$  based on the arrival and departure times according to the schedule, the battery size  $E_b$  of various types of EA, and the energy that needs to be charged  $E_{ch}$  depending on the distance of the previous flight. In addition, an analytical model for constant current–constant voltage (CC–CV) charging strategy is required to simulate  $P_{ch}$ .

### A. Literature Review

In the emerging field of AEA battery power and energy sizing, only a few studies have been conducted thus far. Riboldi and Gualdoni [5] introduced an integrated approach to sizing small AEA. This approach was derived from mission analysis through flight mechanics and design constraints from the sizing matrix. However, it did not account for the power and energy consumption during the takeoff phase. Riboldi [6] employed mathematical models to convert flight performance requirements into constraints for powertrain components. Following this, it introduced an optimal approach to designing small hybrid-EA (HEA), focusing on minimizing takeoff weight. Nevertheless, in the study by Riboldi and Gualdoni [5] and Riboldi [6], only the electric motor and battery weights in the electric powertrain were taken into account

Manuscript received 12 November 2023; revised 28 March 2024 and 24 May 2024; accepted 30 June 2024. Date of publication 15 July 2024; date of current version 3 February 2025. This work was supported in part by the European Union’s Horizon 2020 Research and Innovation Program through the TULIPS Project under Grant 101036996. (Corresponding author: Yawen Liang.)

Yawen Liang, Gautham Ram Chandra Mouli, and Pavol Bauer are with the Electrical Sustainable Energy Department, Delft University of Technology, 2600 AA Delft, The Netherlands (e-mail: y.liang-3@tudelft.nl; g.r.chandramouli@tudelft.nl; p.bauer@tudelft.nl).

Dávid Bodnár is with the Electrical Engineering and Mechatronics Department, Technical University of Košice, 040 01 Košice, Slovakia (e-mail: david.bodnar@tuke.sk).

Daniele Ragni is with the Flow Physics and Technology Department, Delft University of Technology, 2600 AA Delft, The Netherlands (e-mail: D.Ragni@tudelft.nl).

Digital Object Identifier 10.1109/TTE.2024.3427841

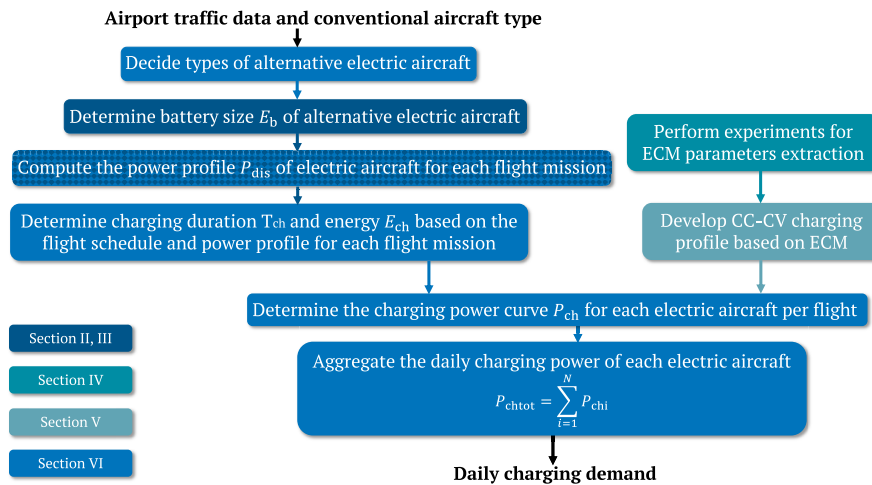


Fig. 1. Workflow of charging demand prediction: AEA and eVTOL aircraft. The solid diamond grid pattern fill represents the combination of Sections II, III, and VI.

TABLE I  
RELATED STUDIES FOR EA BATTERY SIZING

Ref.	Reference aircraft	Takeoff performance	Weight breakdown	Mission analysis
[5]				✓
[6]		✓		✓
[7]		✓		✓
[8]	✓			
[9]	✓		✓	✓
Proposed	✓	✓	✓	✓

when building up the takeoff weight. In [7], the AEA mission power profile, encompassing takeoff, climb, cruise, descent, and reserve phases, was computed using estimated parameters derived from the historical distribution of current aircraft. The takeoff weight is defined based on the typical empty weight fraction observed in current commercial fuel-based aircraft, serving as a potential constraint for this analysis. Gei and Voit-Nitschmann [8] analyzed the boundary conditions governing the battery sizing and designed an energy-optimized HEA based on a reference aircraft. Battery energy was calculated using the Breguet equation, which accounts for cruising energy consumption. This approach is unsuitable for short-range AEA as it does not incorporate energy consumption during takeoff, climb, and descent phases, which are crucial for short-range aircraft. de Vries et al. [9] presented a generic sizing method for HEA, considering the powertrain architecture and associated effects for propulsion-airframe integration. Each powertrain component is represented using a power-loading constraint diagram. However, the takeoff segment is neglected. Despite its short duration and relatively low contribution to the battery size, this phase plays a crucial role in determining the installed aircraft power. The relevant studies are summarized in Table I.

As for the charging demand prediction, numerous studies have focused on predicting the charging demand for electric vehicles (EVs) [10], [11], [12]. However, when it comes to EA, significant differences exist in quantity, battery capacity, and operational strategies compared with EVs. Notably, EVs are subject to customer-driven operational behaviors with a

stochastic nature, whereas EA is centrally managed and highly scheduled [13]. Consequently, a different methodology to predict the charging demands of future EA is needed. The study conducted in [14] analyzed the grid impact of aviation electrification. This analysis was based on the conceptual design of a 180-passenger AEA in [15] with a fixed turnaround time  $T_{ch}$  and constant nominal charging power  $P_{ch}$ . Building upon the same design of the AEA, Schäfer et al. [16] estimated the aggregated annual charging demand of the AEA fleet operating within the global 2015 flight network, while only the global electricity consumption for charging this type of AEA is provided. In study [17], the energy requirement for a short-range narrow-body AEA on a specific mission range  $R$  was calculated using the weight fraction method. The charging duration of AEA was determined by the residual energy level of the battery and the planned range for the next flight. The charging profile  $P_{ch}$  was approximated as a bilinear function of the battery state-of-charge (SOC). Hou et al. [18] quantified the charging requirement of HEA under various battery energy density and motor factor combinations. The study assumed that the HEA arrives at the airport with a depleted battery and needs to be charged to the appropriate level for the next flight with a constant power charging scheme. The required charging power  $P_{ch}$  and energy  $E_{ch}$  were calculated based on flight distance, passenger number, battery energy usage per passenger-mile, and flight schedules. The study in [19] estimated EA charging demand under various passenger demand scenarios using the EV Infrastructure—Energy Estimation and Site Optimization tool to generate representative charging profiles for EA. However, specific information regarding the battery size of EA was not provided. A summary of related studies can be found from Table II.

### B. Scientific Contributions

The main contributions of this article can be summarized as follows.

- 1) A practical battery sizing method for small, short-range AEA aircraft, utilizing a commercial aircraft as a reference, is proposed. Starting with a commercial reference aircraft, this methodology allows for the derivation of

TABLE II  
RELATED STUDIES FOR EA CHARGING DEMAND PREDICTION

Ref.	CC-CV $P_{ch}$	Schedule-based $T_{ch}$	Various EA $E_b$	Flight-distance-based $E_{ch}$
[14]				
[16]		✓		✓
[17]		✓		✓
[18]		✓	✓	✓
[19]	✓	✓		✓
Proposed	✓	✓	✓	✓

high-fidelity assumed aerodynamic coefficients, mission properties, and a design point from real-world performance assessments. This approach also facilitates the accurate determination of the modified operating empty weight (OEW) for AEA. Second, the mission parameters across various flight segments, including takeoff, climb, cruise, descent, and reserve, together with the energy consumption of the auxiliary power unit (APU), are translated to the battery pack weight and detailed powertrain weight, modeled by a chain of critical components. These weight components are aggregated with the payload and the rest of the airframe weights to build up the takeoff weight. This battery sizing method improves upon earlier work by incorporating all design requirements in an integrated and iterative method, including realistic specifications based on the reference aircraft, a detailed component-level partial weights examination to determine takeoff weight, and a detailed mission analysis that encompasses the takeoff phase while adhering to a predefined set of constraints. Table I highlights the improvements of our work over existing work in EA battery sizing.

- 2) Second, an accurate charging demand prediction of future EA is presented, utilizing an analytical model of the CC–CV charging strategy based on the electrical circuit model (ECM) of lithium-ion batteries (LIBs). It considers factors of the turnaround time  $T_{ch}$  available for charging based on the flight schedule, the inclusion of various types of small short-range AEA and eVTOL, and energy consumption per flight  $E_{ch}$  according to the scheduled flight distance and battery power profile during each flight mission, which has not been done earlier. Table II highlights the improvements in our work compared with the existing methods in charging demand estimation.
- 3) This overall methodology is general and adaptable, making it suitable for various types of small, short-range EA, including AEA and eVTOL. It has been validated for 4-, 8-, and 16-seater AEA and 500-kg-payload eVTOL. In addition, it offers an innovative framework that integrates both the battery-discharging power profile during flight missions with the CC–CV charging power profile during airport parking when compared with earlier work, thereby offering a holistic approach to evaluating charging demand across various scenarios.

### C. Paper Structure

This article is structured as follows. The battery sizing methodology for AEA and eVTOL is discussed in Sections II

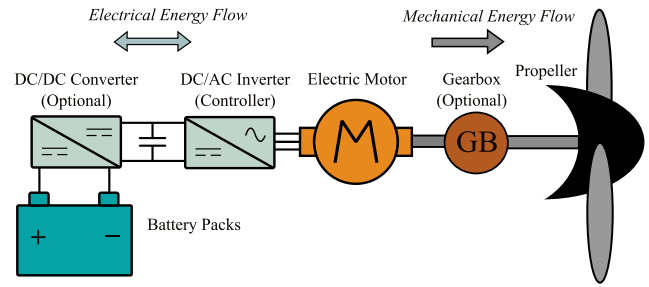


Fig. 2. AEA powertrain architecture schematic [15], [20].

and III, respectively. Section IV covers the ECM of LIBs used for charging power profile prediction. The analytical model of the CC–CV charging profile is presented in Section V. Based on the discussions in Sections II–V, Section VI predicts the charging demand according to the airport traffic data, and different case studies are conducted. Finally, Section VII concludes this article.

## II. BATTERY SIZING FOR AEA

To estimate the charging power demand of AEA, the size of the AEA battery system and the power profile during a typical AEA flight are needed first to acquire the required charging energy after each flight. In this study, aircraft with a passenger capacity of fewer than 20 individuals and a range of up to 250 km are considered. These aircraft are potential candidates for AEA adoption in the coming decade due to their relatively lower battery capacity and energy density requirements [4], [20]. This section elaborates on the battery sizing process for small AEA based on their flight profiles.

### A. All-Electric Propulsion Weight Modifications

When studying AEA, it is crucial to consider the weight penalty associated with the battery energy storage system and subsequent powertrain adjustments. Components such as electric motors and controllers directly impact the OEW of the aircraft. In the conventional fuel-based aircraft propulsion system, the propulsion of the aircraft is performed by the gas turbine engine, while jet fuel is the onboard energy source. For AEA, the electric power sourced from the battery is transmitted to the electric motor, which drives the propeller or fan through a gearbox [15], [20]. Fig. 2 depicts the electric propulsion system architecture in the AEA. In the all-electric propulsion system, battery packs are employed as the onboard energy storage system. An optional dc/dc converter can be incorporated to step up the dc output voltage of battery packs to limit current. A dc/ac inverter serves as a motor controller that utilizes position or speed feedback from the motor to determine both the magnitude and frequency of the output ac voltage. The electric motor converts the ac electric power into mechanical shaft power to propel the propeller. Between the electric motor and the propeller, an intermediate gearbox can be optionally employed by coupling with the high-speed motor, which can effectively reduce the rotational speed and increase the torque applied to the propeller [15].

Each component within the electric propulsion system has a corresponding specific weight. Compared with the conventional baseline aircraft, the transition to electric propulsion

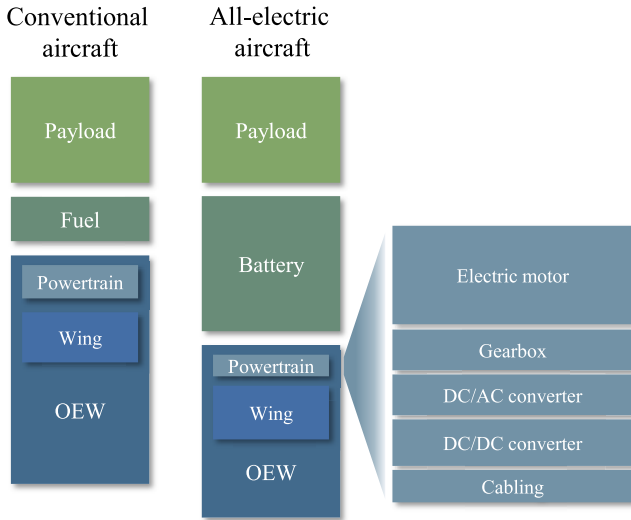


Fig. 3. Weight breakdown comparison between conventional aircraft and retrofit AEA [9].

eliminates the need for fuel and engines but introduces additional mass due to the inclusion of an electric powertrain. Hence, to estimate the takeoff gross weight (TOGW) of an AEA, it is necessary to calculate the weight difference between the baseline conventional fuel-based aircraft and the retrofit AEA. First, as illustrated in Fig. 3, the TOGW of the reference conventional aircraft  $W_{to.ref}$  can be decomposed into fuel weight  $W_f$ , payload weight  $W_{pl.ref}$ , and OEW  $W_{oe.ref}$ . Similarly, the TOGW of the retrofit AEA  $W_{to}$  can be divided into battery weight  $W_b$ , payload weight  $W_{pl}$ , and the modified OEW  $W_{oe}$ , as expressed in (2). Typically, the payload weight is specified as a top-level requirement for an aircraft. Therefore, it is assumed that the payload weight of the retrofit AEA remains the same as that of the reference conventional aircraft

$$W_{to.ref} = W_f + W_{pl.ref} + W_{oe.ref} \quad (1)$$

$$W_{to} = W_b + W_{pl} + W_{oe}. \quad (2)$$

The OEW of the AEA  $W_{oe}$  can be further decomposed to distinguish the contribution of the electric powertrain  $W_{PT}$  from the fuel-based propulsion system, including engine weight  $W_{en}$ . Furthermore, it is essential to isolate the contribution of the wing, as indicated in (3). This expression is based on the assumption that the transition to electric propulsion does not significantly impact the rest of the airframe [9]

$$W_{oe} = W_{oe.ref} - W_{w.ref} - W_{en} + W_{PT} + W_w \quad (3)$$

where  $W_{w.ref}$  and  $W_w$  represent the wing weight of the reference aircraft and retrofit AEA, respectively. Both  $W_{w.ref}$  and  $W_w$  are estimated using the empirical correlation in [21]. The all-electric powertrain weight  $W_{PT}$  consists weight of components, including the electric motor, gearbox, dc/dc converter, dc/ac inverter, and associated cabling, which is sized based on the takeoff power, as this portion has higher power consumption. Thus, the peak power  $P_{peak}$  during the takeoff phase is needed. This requirement can be determined from the design power-loading value ( $P_{peak}/W_{to}$ ), expressed as (4). To meet the certification and mission performance requirement, the target power loading of the retrofit AEA is designed the same as the reference aircraft [5], [6], [9]. Hence,

TABLE III  
STATE-OF-THE-ART TECHNOLOGY FOR ELECTRIC PROPULSION  
SYSTEM COMPONENTS IN AEA

Component	Property	Value
Electric motor	Power density $\rho_{em}$	5 kW kg <sup>-1</sup>
	Efficiency $\eta_{em}$	95%
Gearbox	Power density $\rho_{gb}$	24 kW kg <sup>-1</sup>
	Efficiency $\eta_{gb}$	99%
DC/DC converter	Power density $\rho_{conv}$	26 kW kg <sup>-1</sup>
	Efficiency $\eta_{conv}$	99.5%
DC/AC inverter (controller)	Power density $\rho_{inv}$	26 kW kg <sup>-1</sup>
	Efficiency $\eta_{inv}$	99.5%
Cabling	Power density $\rho_{cabl}$	200 kVA/m · kg
	Efficiency $\eta_{cabl}$	98.5%
Battery pack	Efficiency $\eta_b$	96%

the powertrain weight  $W_{PT}$  can be expressed as (5)

$$P_{peak} = W_{to} \frac{P_{peak.ref}}{W_{to.ref}} \quad (4)$$

$$W_{PT} = P_{peak} \left( \frac{1}{\rho_{em}} + \frac{1}{\rho_{gb}} + \frac{1}{\rho_{conv}} + \frac{1}{\rho_{inv}} + \frac{L_{cabl}}{\rho_{cabl}} \right) \cdot g \quad (5)$$

where  $g$  represents the gravitational acceleration,  $P_{peak.ref}$  and  $W_{to.ref}$  are the engine power and TOGW of the reference aircraft, respectively, and  $\rho_{em}$ ,  $\rho_{gb}$ ,  $\rho_{conv}$ ,  $\rho_{inv}$ , and  $\rho_{cabl}$  are the power density of electric motor, gearbox, dc/dc converter, dc/ac inverter, and cabling respectively. The state-of-the-art technology, in terms of power density and efficiency, for electric propulsion system components in AEA is listed in Table III [15], [22]. To obtain the cable length  $L_{cabl}$ , it is assumed that the batteries would be positioned near the cockpit. This location is chosen because it is closer to the electric motor placed in front of the pilot, which can reduce the length of the cables [23]. There are other possible locations for the battery storage system, such as in the wing or an additional belly pod, but detailed discussions on the weight distribution and center of gravity are beyond the scope of this article.

### B. Battery Sizing Based on Flight Profile

Given the limited amount of available data on AEA, it is necessary to make certain assumptions regarding various factors, including lift coefficient, drag coefficient, and performance indices such as takeoff distance, rate of climb, and cruise speed, to size the battery packs. These parameters are equalized to the corresponding values of the chosen reference conventional aircraft with similar aircraft characteristics. This approach ensures that the same aerodynamic performance, such as drag, can be achieved, which can provide a high degree of confidence and realism to the model [5], [8]. In this study, we select the Cessna 172R as the reference aircraft for the four-seater AEA, which is designed with a cruising range  $R$  of 250 km. Besides the four-seater AEA, 8-seater and 16-seater aircraft are also considered; the reference conventional aircraft is PC-12 and DA-7X, respectively. The specified cruising range for the eight-seater AEA and the 16-seater AEA is set at 200 km. These retrofit AEA are designed with a reduced range compared to the reference aircraft. This is due to the lower specific energy of the battery, resulting in increased energy consumption per mile and ultimately constraining the achievable range. Finally, the commercially available two-seater

TABLE IV  
TECHNICAL SPECIFICATIONS OF CESSNA 172R

Model	Cessna 172R	
	standard	metric
Wing area $S_{ref}$	174 sq ft	16.20 m <sup>2</sup>
Propeller radius $r_{prop}$	38 in	0.9652 m
Propeller speed RPM	2400 rpm	
Propeller number $n_{prop}$	1	
Maximum useful payload $M_{pl,ref}$	758 lbs	344 kg
Standard empty mass $M_{oe,ref}$	1699 lbs	770.61 kg
Takeoff mass $M_{to,ref}$	2450 lbs	1111 kg
Takeoff distance $L_{to}$	945 ft	288.04 m
Rate of climb $V_{v,clb}$	720 ft/min	3.66 m s <sup>-1</sup>
Maximum range	687 nm	1272 km
Cruise speed $V_{cr}$	122 kts	62.76 m s <sup>-1</sup>
Engine dry mass $M_{en}$	258 lbs	117 kg
Engine power $P_{peak,ref}$	160 hp	120 kW
Aspect ratio AR	7.47	
Zero-lift drag coefficient $C_{D0,ref}$	0.031	
Maximum lift coefficient $C_{Lmax,ref}$	1.6	

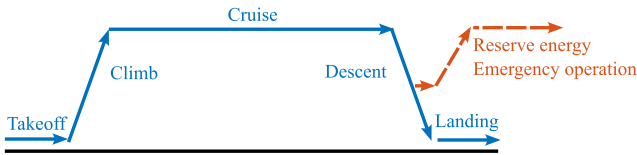


Fig. 4. Illustration of a typical small aircraft mission profile.

Pipistrel Velis Electro aircraft is considered as a replacement for the existing two-seater fuel-based aircraft at the airport.

To demonstrate the battery sizing method for AEA, the Cessna 172 serves as an illustrative example. Technical specifications of Cessna 172 are shown in Table IV [24], [25], [26]. Based on the reference conventional aircraft specifications, the battery pack size for AEA can be estimated by considering various phases of the flight profile. A typical flight profile for a small aircraft consists of five distinct phases: takeoff, climb, cruise, descent, and landing, as shown in Fig. 4. When sizing the battery pack for an AEA, only the first four phases are considered. This is because the landing phase involves minimal energy consumption and lower power requirements [9]. However, AEA batteries must have reserve energy to accommodate unforeseen emergency flight operations, such as balked landings or diversions to alternative locations [27], [28]. Thus, a safety margin is incorporated in the design calculations to account for the energy demands of the landing phase and reserve phase [5], [6]. For the purpose of simplification, the transitional period between flight phases, e.g., from takeoff to climb, is neglected in the following analysis [7].

1) *Takeoff Phase*: The performance requirements of the takeoff phase are often characterized by a specified takeoff run length  $L_{to}$  and takeoff speed  $V_{to}$ . This can be predicted by evaluating the aircraft's acceleration along the runway, which is based on the horizontal force equilibrium, as illustrated in (6). The forces involved in this process include the thrust provided by the propulsion system  $T$ , the aerodynamic drag resisting the aircraft motion  $D$ , and friction  $F$

$$\frac{dV}{dt} = \frac{T - D - F}{M_{to}} \quad (6)$$

where  $\frac{dV}{dt}$  is the linear acceleration along the runway and  $M_{to}$  is the takeoff mass of the designed AEA. During the takeoff phase, it is reasonable to assume that the motor power remains relatively constant. A practical approach is to utilize the maximum motor power  $P_{em}$  values provided by the manufacturer for takeoff calculations [7]. In practice, for scenarios involving multiple motors, the total maximum motor power  $P_{em}$  is determined by summing the maximum power of each individual motor.

Thrust  $T$  varies with velocity  $V$  and propeller efficiency  $\eta_{prop}$ , which exhibit significant changes throughout the takeoff. Thrust is calculated as follows:

$$T = \frac{P_{em}}{\eta_{prop}\eta_{em}\eta_{gb}V}. \quad (7)$$

During the takeoff phase, the propeller efficiency  $\eta_{prop}$  is determined by the thrust coefficient  $T_c$ , as calculated in (8), which takes into account the aircraft velocity  $V$ , thrust  $T$  at the current aircraft state, the number of propellers  $n_{prop}$ , the propeller radius  $r_{prop}$  of the aircraft, and the air density during takeoff  $\rho^{to}$  which represents the field elevation of the airport

$$\eta_{prop} = \frac{2}{1 + \sqrt{1 + T_c}}$$

$$T_c = \frac{2T}{n_{prop}\rho^{to}V^2\pi r_{prop}^2}. \quad (8)$$

Except for the propeller efficiency during the takeoff phase, one approximation made in this study is assuming constant efficiencies for other powertrain components, such as electric motors. This assumption is reasonable for high-level preliminary studies since the use of an electric drive and active control enables the propeller to operate closely to its maximum efficiency point for every flight condition [29].

The aerodynamic drag  $D$  experienced by the aircraft is dependent on its velocity  $V$ . To derive the aerodynamic drag  $D$ , parabolic drag polar is assumed, as expressed in the following equation:

$$D = \frac{1}{2}\rho^{to}V^2S(C_{D0}^{to} + K_{to}C_L^{to2}) \quad (9)$$

where  $S$  is the wing area of the retrofit aircraft,  $C_{D0}^{to}$  is the zero-lift drag coefficient during takeoff,  $K_{to}$  is the induced drag correction factor during takeoff, and  $C_L^{to}$  is the lift coefficient during takeoff.  $K_{to}$  for straight wings can be calculated as a function of Oswald span efficiency factor  $e$  and the aspect ratio AR, which is the ratio of the wing span squared to the wing area  $S$  [21].

The friction  $F$  can be expressed as a function of the friction coefficient  $\mu$ , which is determined by the tire-surface interaction. The friction  $F$  is proportional to the difference between the aircraft weight  $W_{to}$  and the current lift force. This relationship can be represented as follows:

$$F = \mu \left( W_{to} - \frac{1}{2}\rho^{to}V^2SC_L^{to} \right). \quad (10)$$

Based on (6), (7), (9), and (10), the takeoff time  $T_{to}$  can be calculated. Therefore, the battery energy consumption for takeoff  $E_{to}$  can be estimated using (11). The total efficiency stack up of the electrical propulsion system, denoted by  $\eta_E$ , is the product of the individual efficiencies  $\eta_b$ ,  $\eta_{conv}$ ,  $\eta_{inv}$ , and  $\eta_{cabl}$

$$E_{to} = \frac{P_{em}}{\eta_E} T_{to}. \quad (11)$$

2) *Climb and Descent Phases*: During the climb and descent phase, it is assumed that the acceleration of the aircraft is negligible [29]. Therefore, the expression of climb  $P_{\text{clb}}$  and descent power  $P_{\text{des}}$  can be obtained based on the equilibrium of all the forces acting upon an aircraft [30]

$$\begin{aligned} P_{\text{clb}} &= W_{\text{to}} V_{\text{v,clb}} + \left( \frac{1}{2} \rho^{\text{clb}} S V_{\text{clb}}^3 C_{\text{D0}}^{\text{clb}} + K^{\text{clb}} \frac{W_{\text{to}}^2}{\frac{1}{2} \rho^{\text{clb}} S V_{\text{clb}}} \right) \\ P_{\text{des}} &= W_{\text{to}} V_{\text{v,des}} + \left( \frac{1}{2} \rho^{\text{des}} S V_{\text{des}}^3 C_{\text{D0}}^{\text{des}} + K^{\text{des}} \frac{W_{\text{to}}^2}{\frac{1}{2} \rho^{\text{des}} S V_{\text{des}}} \right) \end{aligned} \quad (12)$$

where  $V_{\text{v,clb}}$  is the rate of climb, which represents the rate of altitude change with respect to time.  $\rho^{\text{clb}}$  is the air density during the climb phase, which is assigned the average value between the air density at takeoff and the air density at cruising altitude.  $V_{\text{clb}}$  is the aircraft velocity during the climb phase.  $C_{\text{D0}}^{\text{clb}}$  and  $K^{\text{clb}}$  are the zero-lift drag coefficient and induced drag correction factor during the climb phase, respectively. Similarly,  $V_{\text{v,des}}$ ,  $\rho^{\text{des}}$ ,  $V_{\text{des}}$ ,  $C_{\text{D0}}^{\text{des}}$ , and  $K^{\text{des}}$  represent the rate of descent, air density, and the aircraft velocity, zero-lift drag coefficient, and induced drag correction factor during the descent phase, respectively.

Similar to (11), the battery energy consumption during the climb and descent phases can be computed as (13). During the climb, descent, and cruising phase, the propeller efficiency  $\eta_{\text{prop}}$  is assumed to be constant at 0.8. The time duration of the climb and descent phases can be calculated based on the vertical distance difference  $\Delta h$  between the takeoff or landing and cruising altitude

$$\begin{aligned} E_{\text{clb}} &= \frac{P_{\text{clb}}}{\eta_E \eta_{\text{em}} \eta_{\text{gb}} \eta_{\text{prop}}} \cdot \frac{\Delta h}{V_{\text{v,clb}}} \\ E_{\text{des}} &= \frac{P_{\text{des}}}{\eta_E \eta_{\text{em}} \eta_{\text{gb}} \eta_{\text{prop}}} \cdot \frac{\Delta h}{V_{\text{v,des}}} \end{aligned} \quad (13)$$

3) *Cruising and Reserve Phases*: The cruise power can be expressed as follows:

$$P_{\text{cr}} = \frac{1}{2} \rho^{\text{cr}} S V_{\text{cr}}^3 C_{\text{D0}}^{\text{cr}} + K^{\text{cr}} \frac{W_{\text{to}}^2}{\frac{1}{2} \rho^{\text{cr}} S V_{\text{cr}}} \quad (14)$$

where  $V_{\text{cr}}$  is the aircraft cruising speed.  $\rho^{\text{cr}}$  is the air density during the cruising phase, and  $C_{\text{D0}}^{\text{cr}}$  and  $K^{\text{cr}}$  are the zero-lift drag coefficient and induced drag correction factor during the cruise phase, respectively.

The energy consumption of the cruise phase can be determined based on the specified cruising range requirements  $R$  and cruise speed  $V_{\text{cr}}$ , as shown in the following equation:

$$E_{\text{cr}} = \frac{P_{\text{cr}}}{\eta_E \eta_{\text{em}} \eta_{\text{gb}} \eta_{\text{prop}}} \cdot \frac{R}{V_{\text{cr}}} \quad (15)$$

As stated earlier, the provision of reserve energy is essential for safety purposes. In the case of short-haul small AEA, a reserve cruise time of 15 min, denoted by  $T_{\text{res}}$ , is considered. Assuming that the reserve cruise phase aligns with the normal cruise phase, the reserve energy, denoted by  $E_{\text{res}}$ , can be calculated using the following formula:

$$E_{\text{res}} = \eta_E \eta_{\text{em}} \eta_{\text{gb}} \eta_{\text{prop}} T_{\text{res}} \cdot \quad (16)$$

In addition to the energy utilized for propulsion, an APU consumes energy to provide autonomous electrical and

TABLE V

PERFORMANCE INDICES OF RETROFIT CESSNA 172R [3], [6], [35]

Model	Retrofit Cessna 172R
Friction coefficient $\mu$	0.03
Lift coefficient during takeoff $C_L^{\text{to}}$	1.6
Zero-lift drag coefficient $C_{\text{D0}}^{\text{to}}, C_{\text{D0}}^{\text{clb}}, C_{\text{D0}}^{\text{des}}, C_{\text{D0}}^{\text{cr}}$	0.031
Rate of descent $V_{\text{v,des}}$	-3.66 m s <sup>-1</sup>
Climb/Descent speed $V_{\text{clb}}, V_{\text{des}}$	62.87 m s <sup>-1</sup>
Cruise range $R$	250 km
Field elevation of the airport $h_a$	-3.4 m
Cruise altitude $h_{\text{cr}}$	1219.2 m
Air density (takeoff) $\rho^{\text{to}}$	1.225 kg m <sup>-3</sup>
Air density (climb and descent) $\rho^{\text{clb}}, \rho^{\text{des}}$	1.157 kg m <sup>-3</sup>
Air density (cruise and reserve) $\rho^{\text{cr}}$	1.088 kg m <sup>-3</sup>
Battery pack energy density $e_b$	300 Wh kg <sup>-1</sup>
Battery pack power density $\rho_b$	800 W kg <sup>-1</sup>

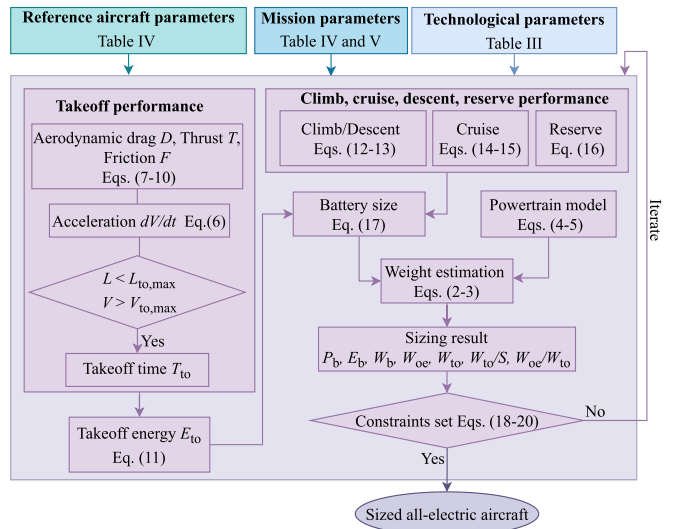


Fig. 5. Flowchart of the AEA sizing procedure.

mechanical power. Typically, the APU's energy consumption, denoted by  $E_{\text{apu}}$ , constitutes up to 2% of the total energy usage during a typical flight [31]. Hence, the battery pack size for the AEA can be computed as follows:

$$E_b = E_{\text{to}} + E_{\text{clb}} + E_{\text{cr}} + E_{\text{des}} + E_{\text{res}} + E_{\text{apu}} \quad (17)$$

### C. Analysis of the Set of Constraints

Based on the mission performance requirement, polar coefficients for various flight phases in Tables IV and V, and the relationship between weight components and mission requirements in (2)–(17), the system encompassing  $W_{\text{to}}$  and  $W_{\text{oe}}$  and  $W_b$  can be closed. An iterative calculation is performed to determine the TOGW and battery pack size of the retrofit AEA based on the Cessna 172R while adhering to a set of constraints to ensure the validity of the retrofit design, including the empty weight ratio, the wing loading, and the battery power constraints. The flowchart of the battery sizing procedure is shown in Fig. 5.

1) *Empty Weight Ratio*: The first constraint is the statistical logarithmic relationship between  $W_{\text{oe}}$  and  $W_{\text{to}}$ , as expressed in (18). The coefficient for the weight regression is estimated using data from a collection of small AEA for general aviation

[5], [6], [21], while  $A = 0.6694$ ,  $B = -0.052$ , and  $K_{vs} = 1$  for fixed wing.

Because the dataset for AEA in the regression equation (18) is limited, there are uncertainties in the equation coefficients. To manage this, a mathematical formulation with two inequality constraints is employed. This formulation specifies that the solution can stay within a defined distance from the regression line on  $W_{to}$  and  $W_{oe}$ . Two relative distances are introduced,  $\xi_{upper}$  and  $\xi_{lower}$ , which can be specified as 1.15 and 0.85, respectively. These tolerance factors define the maximum acceptable deviation of the design solution from the regression line

$$\xi_{lower} \cdot A(W_{to})^C K_{vs} \leq \frac{W_{oe}}{W_{to}} \leq \xi_{upper} \cdot A(W_{to})^C K_{vs} \quad (18)$$

2) *Wing Loading*: The second constraint is about the choice of design point in terms of wing loading ( $W_{to}/S$ ), which is the weight of the aircraft divided by the wing area. Similar to power loading, wing loading has a significant impact on various performance calculations, influencing factors, such as stall speed, climb rate, takeoff, and landing distances, and turn performances [21]. Hence, to obtain a comparable mission performance, the wing loading is selected to be the same as that of the reference conventional aircraft, allowing for a permissible variation defined by parameters  $\theta_{lower}$  and  $\theta_{upper}$ . These parameters are set to 0.85 and 1.15, respectively,

$$\theta_{lower} \cdot \frac{W_{to,ref}}{S_{ref}} \leq \frac{W_{to}}{S} \leq \theta_{upper} \cdot \frac{W_{to,ref}}{S_{ref}}. \quad (19)$$

3) *Maximum Battery Pack Power*: The third constraint pertains to the battery pack's ability to handle the maximum power requirement. Specifically, it involves an inequality constraint on the power flow within the battery. This constraint guarantees that the battery power, denoted by  $P_b$ , must always remain below the threshold determined by the power density of the selected battery technology, denoted by  $\rho_b$

$$\max P_b \leq \frac{W_b \rho_b}{g}. \quad (20)$$

#### D. Methodology Verification

To validate the proposed methodology, a comparative analysis of the power and energy profiles of the designed all-electric retrofit Cessna 172R and Pipistrel Velis Electro was conducted. Using the ‘‘Electrical Component Analysis for Hybrid and Electric Aircraft’’ tool in MATLAB/Simulink, the aircraft was modeled as 4th-order point masses (longitudinal) in flight, with the required thrust output serving as a load on the motor [32]. As illustrated in Fig. 6, the average climb, cruise, and descent power based on Simulink simulation  $P_{SL}$  are 223.01 kW, 132.15 kW, and 56.03 kW, respectively. The simulated energy demand for a typical flight mission was 246.93 kWh, whereas the energy requirement derived from the proposed methodology was 249.44 kWh. For the Pipistrel Velis Electro, based on the performance and weight indices provided in [33], the power and energy profiles according to the proposed method, Simulink model, and [33]  $P_{DS}$  were given in Fig. 7. The calculated power and energy of the proposed model are slightly higher than the datasheet and Simulink result.

As for the difference between the Simulink model and the proposed method, both in the retrofit Cessna and Velis

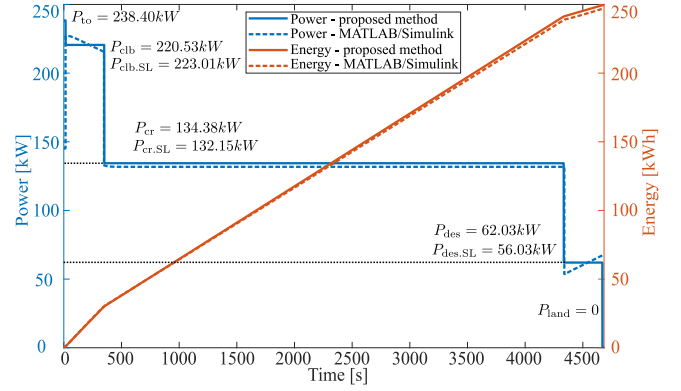


Fig. 6. Power and energy profile of the retrofit Cessna 172R.

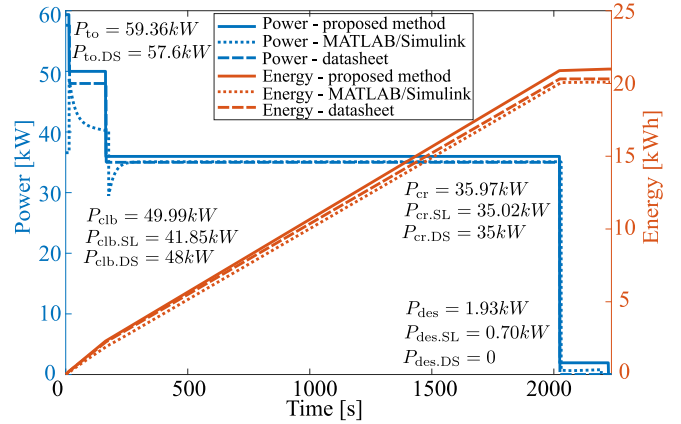


Fig. 7. Power and energy profile of the Pipistrel Velis Electro.

Electro, it can be ascribed to the Simulink model's incorporation of the lift coefficient's dependence on the angle of attack. Furthermore, the takeoff phase is not modeled in the Simulink simulation, while this is included in the proposed method. For the difference between the proposed method and datasheet for Velis Electro, the estimated battery sizes are 26.63 kWh for Velis Electro, which slightly deviates from the rated capacities of 24 kWh, respectively. Potential explanations for this could be the fluctuating efficiency during flight missions and variations in the aerodynamic coefficient values. By summing up the battery pack weight, payload weight, powertrain weight, and the remaining OEW, the estimated takeoff weight determined using the proposed method is 618.36 kg, which is slightly higher than the actual 600 kg. This can be attributed to the increased battery pack weight. In addition, the increased takeoff weight elevates the powertrain weight due to the higher peak power, alongside an increase in energy consumption during flight. The proposed iterative sizing method also indicates such interplay among these weight components, where alterations in one component can significantly impact the others.

To further validate the proposed method, the Elysian aircraft were selected. Based on the performance and weight indices provided in [34], the battery sizing methodology was utilized to assess the takeoff weight and energy consumption across various flight phases. By aggregating these energy consumption components, the estimated battery size for Elysian is 15631.5 kWh, slightly deviating from the rated capacity of

TABLE VI  
TECHNICAL SPECIFICATIONS OF THE RETROFIT AEA

Model	Retrofit Cessna 172R	Retrofit PC-12
Battery size $E_b$	302.94 kW h	1743.06 kW h
Battery pack mass $M_b$	1009.80 kg	5810.19 kg
Operating empty mass $M_{oe}$	853.36 kg	3693.31 kg
Takeoff mass $M_{to}$	2207.15 kg	9961.51 kg
Wing loading $\frac{W_{to}}{S}$	773.57 N m <sup>-2</sup>	2071.71 N m <sup>-2</sup>
Power loading $\frac{P_{peak}}{W_{to}}$	0.091 N W <sup>-1</sup>	0.052 N W <sup>-1</sup>
Empty weight fraction $\frac{W_{oe}}{W_{to}}$	0.39	0.37

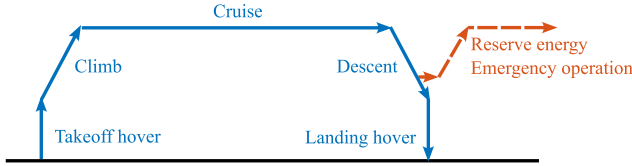


Fig. 8. Schematic of a typical eVTOL trip.

15382.4 kWh. This can be attributed to the same reasons as those for the Pipistrel Velis Electro.

### E. Sizing Result

Given the successful verification and demonstrated high accuracy, the proposed sizing method is applied to size the battery of the retrofit PC-12 and DA-7X, and the technical specifications of the all-electric retrofit Cessna 172R and PC-12 are listed in Table VI. These specifications include important details, such as battery size and takeoff mass. Regarding the retrofit DA-7X, a solution satisfying all the constraints cannot be found based on an energy density of 300 W·h·kg. The threshold for a feasible 16-seater AEA with 200 km is 360 W·h·kg at the pack level, which indicates a trend of increasing demand for gravimetric battery energy density as aircraft size grows. The calculated takeoff mass is 77039.2 kg, with a corresponding battery size of 16842.4 kWh.

## III. BATTERY SIZING FOR EVTOL AIRCRAFT

Alongside conventional takeoff and landing AEA in Section II, eVTOL aircraft can also be utilized at airports, for instance, as medical helicopters. The eVTOL aircraft can take off and land vertically like helicopters, allowing for more flexible operations, as they do not require a runway or large landing area.

### A. Power Requirements

To determine the battery size for eVTOL aircraft, detailed power and energy calculations for each phase of flight are necessary. A typical eVTOL trip, as illustrated in Fig. 8, involves five distinct phases: takeoff hover, climb, cruise, descent, and landing hover [27]. In addition, similar to AEA, eVTOL aircraft require reserve energy. This design assumes a 15 min reserve for the additional cruise.

First, the hover power during the takeoff and landing phases is modeled based on momentum theory, as shown in the following equation [1]:

$$P_{\text{hover}}^V = \frac{W_{to}^V}{\mu_h^V} \sqrt{\frac{\sigma}{2\rho^{to}}} \quad (21)$$

where  $W_{to}^V$  is the gross takeoff weight of the eVTOL, and  $\mu_h^V$  is the hover efficiency, which is a lumped parameter that depends on the figure of merit, fuselage down-wash correction, and combined mechanical efficiency of motors and electric powertrain [27].  $\sigma$  is the disk loading.

In climb, descent, and reserve phases, a general expression for the required power can be derived by referencing basic static equilibrium equations from flight mechanics [1], [36]

$$P_i^V = \frac{W_{to}^V}{\mu_s^V} \left( V_{\text{roi}}^V + \frac{V_i^V}{(L/D)_i} \right) \quad (22)$$

where  $V_{\text{roi}}^V$  denotes the vertical velocity, which is 0 during cruise and reserve phases.  $V_i^V$  is the true airspeed,  $(L/D)_i$  is the lift-to-drag ratio, and  $\mu_s^V$  is the overall system efficiency, which is the product of the propeller efficiency and combined mechanical efficiency. The subscript roi and i denote each flight phase.

The gross takeoff weight of the eVTOL aircraft is defined as the sum of its OEW ( $W_{oe}^V$ ), payload ( $W_{pl}^V$ ), and battery weight ( $W_b^V$ ), as shown in (23). The OEW  $W_{oe}^V$  can be calculated using the empty weight ratio  $K_{\text{EWF}}^V = W_{oe}^V / W_{to}^V$

$$W_{to}^V = W_{pl}^V + W_b^V + K_{\text{EWF}}^V W_{to}^V \quad (23)$$

### B. Sizing Result

Therefore, the total battery energy required for an eVTOL trip can be calculated by integrating the specific power required for each flight phase over time, which is based on the specified performance requirements and lift-to-drag ratio for various flight phases in Table VII

$$E_b^V = \sum_i P_i^V T_i^V + E_{\text{apu}}^V \quad (24)$$

where  $T_i^V$  represent the time duration for each flight phase. Similar to AEA in Table II,  $E_{\text{apu}}^V$  is used to account for the energy consumed by the APU. The flowchart of the eVTOL sizing procedure is shown in Fig. 9. The sizing iteration concludes when the empty weight ratio matches the preset value  $K_{\text{EWF}}^V$ . The resulting mass properties and battery size of the designed eVTOL are shown in Table VIII. The power profile is illustrated in Fig. 10, presenting the power requirements and energy consumption across various mission segments, encompassing takeoff hover, climb, cruise, descent, and landing hover phases.

## IV. ELECTRICAL CIRCUIT MODEL

Currently, the most widely adopted charging method is the CC–CV charging strategy [37]. As illustrated in Fig. 11, in the constant current (CC) phase, the battery is initially charged with a controlled CC  $I_C$ , while the battery voltage  $V$  increases gradually. Once reaching the cutoff voltage  $V_C$ , the charging process switches into the constant voltage (CV) phase. During the CV phase,  $V$  keeps constant at  $V_C$ , and the charging current  $I$  decreases gradually. The charging process is terminated when charging current  $I$  drops below the preset level  $I_D$ , typically 0.02C [38]. To predict the charging demand of AEA and eVTOL with CC–CV charging method under different operational conditions precisely, battery models with accurate model parameters are essential.

TABLE VII  
PERFORMANCE INDICES OF THE eVTOL [27], [36]

Model	eVTOL
Maximum range	250 km
Disk loading $\sigma$	490 N m <sup>-2</sup>
Hover efficiency $\eta_h^V$	0.64
Overall system efficiency $\eta_s^V$	0.85
Lift-to-drag ratio (climb/descent) $(L/D)_{clb/des}$	12
Lift-to-drag ratio (cruise/reserve) $(L/D)_{cr/res}$	14
Empty weight fraction $K_{EWF}^V$	0.60
Takeoff/Landing duration $T_{to}^V, T_{land}^V$	30 s
Climb/Descent duration $T_{clb}^V, T_{des}^V$	120 s
Reserve duration $T_{res}^V$	900 s
Climb/Descent true airspeed $V_{clb}^V, V_{des}^V$	50 m s <sup>-1</sup>
Rate of climb $V_{roc}^V$	2.54 m s <sup>-1</sup>
Rate of descent $V_{rod}^V$	-2.54 m s <sup>-1</sup>
Cruise true airspeed $V_{cr}^V$	66.67 m s <sup>-1</sup>

TABLE VIII  
TECHNICAL SPECIFICATIONS OF THE DESIGNED eVTOL

Description	Value
Battery size $E_b^V$	292.77 kW h
Battery pack mass $M_b^V$	975.90 kg
Payload mass $M_{pl}^V$	500 kg
Operating empty mass $M_{oe}^V$	2213.85 kg
Takeoff mass $M_{to}^V$	3689.75 kg

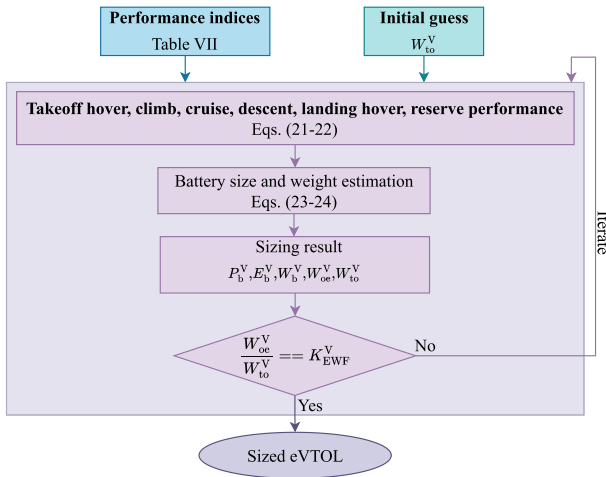


Fig. 9. Flowchart of the eVTOL sizing procedure.

This study uses the second-order RC Thévenin-based model to simulate the battery behavior, as depicted in Fig. 12. This ECM comprises several components: the open-circuit voltage (OCV)  $V_{OCV}$ , the ohmic resistance  $R_o$ , the short-time transient parallel RC pair  $R_s$  and  $C_s$ , and the long-time transient components  $R_l$  and  $C_l$ . These model parameters are multivariable functions that depend on various factors, including the SOC, ambient temperature ( $T$ ), current direction and C-rate, battery aging levels, self-discharge rate, and hysteresis effects [39]. Therefore, these parameters must be carefully determined and calibrated to accurately represent the battery behavior in different operating environments.

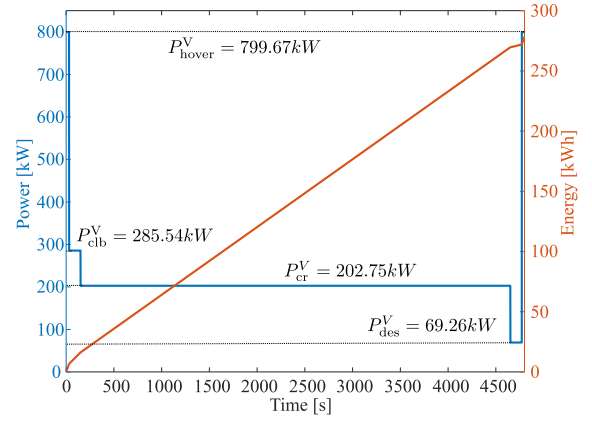


Fig. 10. Power and energy profile of the designed eVTOL.

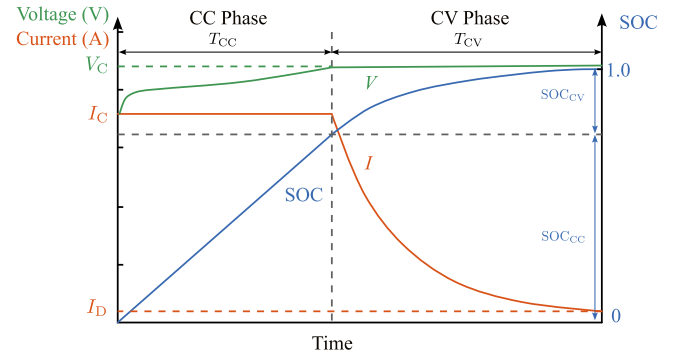


Fig. 11. CC-CV charge profile.

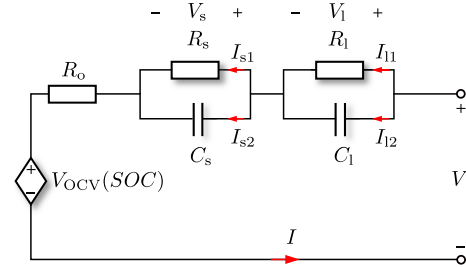


Fig. 12. Second-order RC Thévenin-based model.

### A. Experimental Setup

Considerable attention has been focused on enhancing battery performance, particularly in achieving higher energy density. For instance, lithium-sulfur batteries (LSBs) utilize nanostructured sulfur/carbon composites with conductive carbon in large quantities as cathodes, combined with lithium metal as anodes. This technology offers high gravimetric energy (500 W·h·kg) with low-cost sulfur. Theoretical projections suggest that LSBs have the potential to achieve a significantly high energy density of approximately 2600 W·h·kg [3]. Nevertheless, lithium nickel manganese cobalt oxides (NMC)-type LIBs are expected to dominate air transportation in the near-term future [40]. For instance, the two-seat Pipistrel Velis Electro AEA relies on two battery packs composed of cylindrical LIB cells utilizing NMC

TABLE IX  
KEY PARAMETERS FOR THE INR18650-35E BATTERY

Parameter	Value
Model name	Samsung INR18650-35E
Format	Cylindrical cell
Nominal capacity [A h]	3.4
Max. voltage [V]	4.2
Nominal voltage [V]	3.6
Charge operating temperature [°C]	0 to 45
Gravimetric energy density [W h kg <sup>-1</sup> ]	244.8
Standard charging method	CC-CV 1.7 A, 4.2 V max. 68 mA cut-off

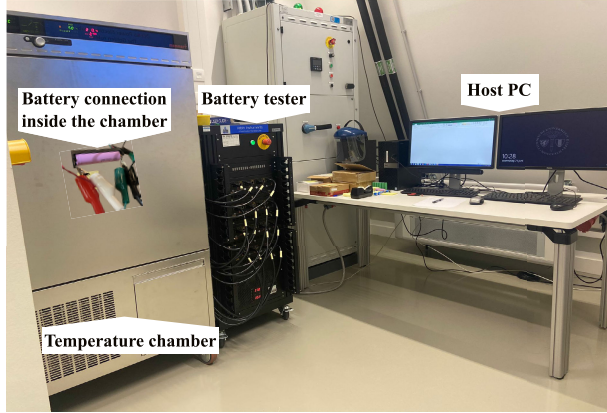


Fig. 13. Experimental setup for battery tests.

chemistry [33]. This is primarily due to their well-established technology and strong battery supply chain, making them a viable choice for immediate implementation. In this study, the Samsung INR18650-35E cylindrical cell is chosen for ECM parameter extraction, which represents the NMC technology of LIBs. The key parameters of the tested battery cell are outlined in Table IX [41]. Fig. 13 illustrates the experimental setup used for battery ECM testing. The setup comprises a battery tester (16 channels, each rated for 25 V, 10 A), a temperature chamber to regulate the ambient temperature during tests, and a host PC responsible for monitoring, controlling the test, and recording the test data. All the collected data are input into MATLAB for the ECM parameter extraction.

## B. Test Procedure

1) *Internal Impedance Measurements*: The values for the circuit components of the ECM were determined using a similar methodology as described in [39] and [42], as illustrated in Fig. 14. Due to the primary varying parameters during the CC-CV charging process, namely, SOC, C-rate, and temperatures of the battery cell, the same test profile was repeated at different C-rate ranging from 0.2C to 1.0C and ambient temperatures, including 0 °C, 10 °C, 20 °C, 25 °C, 30 °C, and 40 °C, for three INR18650-35E cells. The ECM parameters for each operating condition were then extracted from the corresponding pulse test characterization results, as explained in Section IV-C.

2) *OCV Measurements*: The OCV at equilibrium was determined using a similar test procedure as shown in Fig. 14. However, the resting period was extended to 3 h instead of 180 s to measure the close-to-equilibrium OCV for both

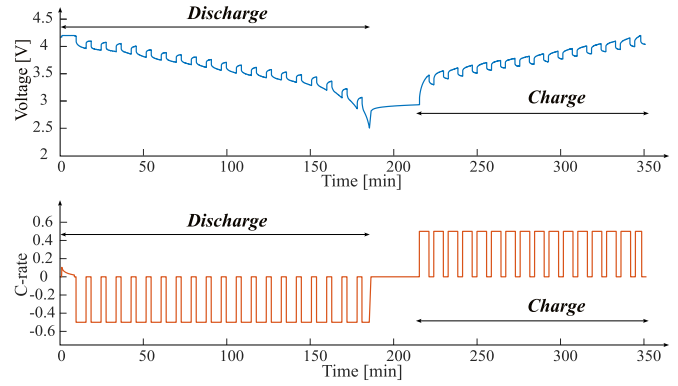


Fig. 14. Voltage and current profile for the test cycle.

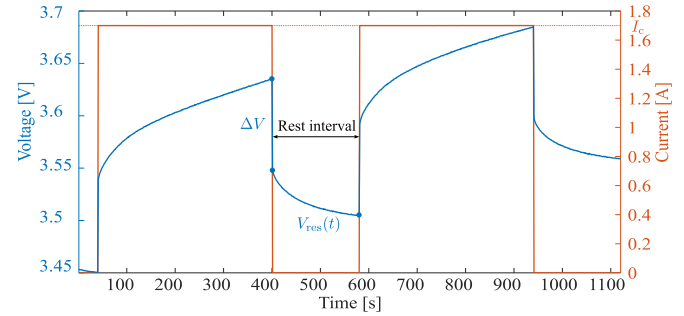


Fig. 15. Zoomed voltage and current profile during charging test cycles.

discharging and charging. It is noted that the temperature fluctuations of OCV-SOC were found to be negligible in moderate SOC levels, suggesting that the OCV can be considered as temperature-independent [39], [42]. Therefore, specific OCV tests under different temperature conditions were not conducted without any noticeable effects on model accuracy in this study.

## C. Extraction of ECM Parameters

To establish the dependency of ECM parameters on SOC,  $T$ , and C-rate, curve fitting is performed during the rest interval between charging or discharging pulses. This is because during the rest interval, the SOC remains constant, and the load current is 0 [39]. As shown in Fig. 15, the internal ohmic resistance  $R_0$  can be determined based on the immediate voltage drop  $\Delta V$ . The component values of short-time and long-time transient parallel  $RC$  pairs are established by curve fitting the remaining voltage response  $V_{res}(t)$ .

1) *Open-Circuit Voltage Modeling*: Since the focus is on the charging power profile modeling, only the OCV-SOC curve and ECM parameter variations relevant to the charging process are considered. The OCV-SOC curve is illustrated in Fig. 16.

2) *Internal Impedance Modeling*: Figs. 17 and 18 present the ECM parameter variations with  $T$  and C-rate under the charging process, respectively. As shown in Figs. 17(a) and 18(a),  $R_0$  values increased when the temperature and C-rate are lower. Likewise, as the temperature increased, the values of  $R_s$  and  $R_1$  dropped, while the values of  $C_s$  and  $C_1$  increased. As to the C-rate dependence, a downward trend with C-rate of  $R_0$ ,  $R_s$ , and  $R_1$  values could be observed.

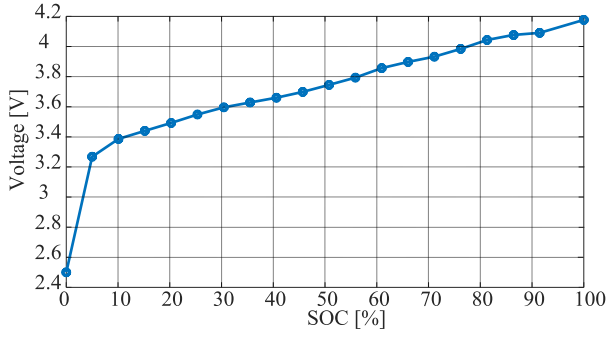
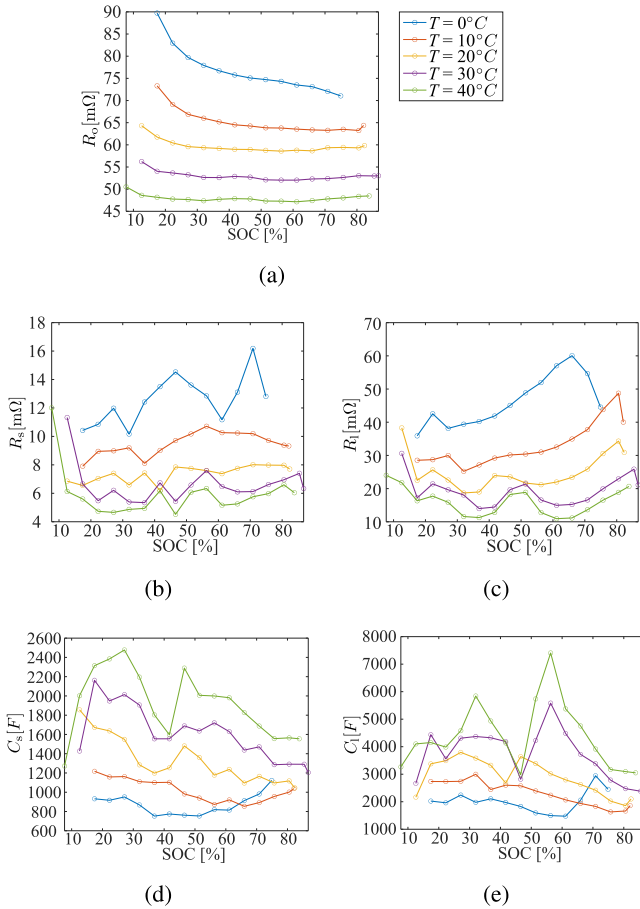


Fig. 16. OCV-SOC relation under charging process.

Fig. 17. ECM parameter variations with  $T$  under charging process. (a)  $R_o$ . (b)  $R_s$ . (c)  $R_l$ . (d)  $C_s$ . (e)  $C_l$ .

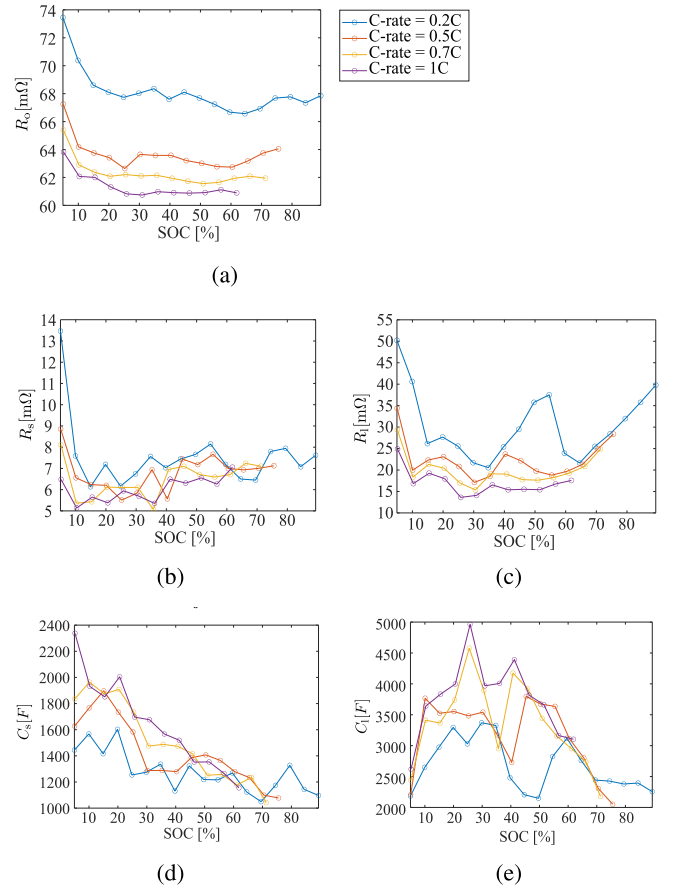
## V. ANALYTICAL MODEL FOR CC-CV CHARGING PROCESS

Based on the ECM described in Section IV, an analytical model for the CC-CV charging process is necessary to accurately simulate the charging power during both CC and CV phases.

### A. CC Phase

As depicted in Fig. 12, the cell terminal voltage  $V(t)$  can be expressed as the sum of two RC pair voltages ( $V_s(t)$  and  $V_l(t)$ ), the constant charging current  $I_C$  multiplying  $R_o$ , and  $V_{ocv}(t)$ , as illustrated in the following equation:

$$V(t) = V_l(t) + V_s(t) + I_C R_o + V_{ocv}(t). \quad (25)$$

Fig. 18. ECM parameter variations with C-rate under charging process. (a)  $R_o$ . (b)  $R_s$ . (c)  $R_l$ . (d)  $C_s$ . (e)  $C_l$ .

Notice resistor  $R_s$  or  $R_l$  do not carry the full charging current. The charging current is split between the resistor currents  $I_{s1}$  and  $I_{l1}$  and the capacitor currents  $I_{s2}$  and  $I_{l2}$ . To derive the expression for the current flowing through the resistor in the parallel RC branch, the transient behavior of the short-time RC pair is considered as an illustrative example

$$\begin{aligned} I_C &= I_{s1}(t) + I_{s2}(t) \\ I_{s2}(t) &= C_s \frac{dV_s(t)}{dt} = R_s C_s \frac{dI_{s1}(t)}{dt} \\ \frac{dI_{s1}(t)}{dt} &= \frac{I_C}{R_s C_s} - \frac{I_{s1}(t)}{R_s C_s}. \end{aligned} \quad (26)$$

Based on (26), the parallel RC pair voltage can be written in a different way as the voltage across resistor  $R_s$  or  $R_l$ . Thus, an alternative representation of the cell terminal voltage  $V$  can be formulated as follows:

$$\begin{aligned} I_{l1}(t) &= I_C \left(1 - e^{-\frac{t}{R_l C_l}}\right) \\ I_{s1}(t) &= I_C \left(1 - e^{-\frac{t}{R_s C_s}}\right) \\ V(t) &= I_{l1}(t) R_l + I_{s1}(t) R_s + I_C R_o + V_{ocv}(t). \end{aligned} \quad (27)$$

### B. CV Phase

During the CV phase, the charging current  $I(t)$  is no longer constant, which can introduce additional complexity to the model. The equations for the ECM are shown as follows:

$$I_{l1}(t) R_l = \frac{1}{C_l} \int (I(t) - I_{l1}(t)) dt + V_{l2,0}$$

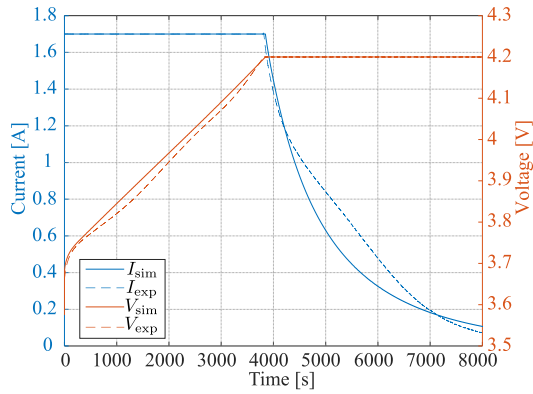


Fig. 19. Comparison of the measured and simulated current and voltage results.

$$I_{s1}(t)R_s = \frac{1}{C_s} \int (I(t) - I_{s1}(t))dt + V_{s2,0}$$

$$V_C = V_{OCV}(t) + I(t)R_o + I_{s1}(t)R_s + I_{l1}(t)R_l \quad (28)$$

where  $V_{l2,0}$  and  $V_{s2,0}$  are the initial voltage value of the short-time transient parallel  $RC$  pair and the long-time transient parallel  $RC$  pair, respectively.

### C. Verification of the Charge Profile Prediction

Based on (27) and (28), the CC–CV charging profile can be modeled utilizing the extracted ECM parameters in Section IV. To validate the proposed model's accuracy, a battery cell was charged with the CC–CV strategy at 0.5C. The ambient temperature was set to a constant value of 25 °C, which was maintained using a temperature chamber. The simulated voltage  $V_{sim}$  and current  $I_{sim}$  profiles obtained from the model were compared with the voltage  $V_{exp}$  and current  $I_{exp}$  measurements obtained from the battery experiment. The comparison results are shown in Fig. 19. The close agreement between the measured and simulated curves demonstrates the accuracy of the model in predicting the CC–CV charging profile. The root-mean-square percentage error (RMSPE) for current and voltage predictions was 0.8282% and 0.0174%, respectively. In addition to the 25 °C operating point, the CC–CV charging test was also conducted at 20 °C ambient temperature, yielding an RMSPE value below 1%.

## VI. CHARGING DEMAND PREDICTION

Based on the previous discussions in Sections II–V, the future charging demand at airports, stemming from the integration of various AEA and eVTOL, can be forecasted using the airport's flight schedule. First, the performance requirements of conventional aircraft are assessed. If the payload requirement and flight distance fall within the operational capabilities of the designed AEA and eVTOL, they will replace the conventional aircraft for that flight. It is worth noting that the total flight distance of AEA and eVTOL includes not only the cruising range  $R$  but also the horizontal displacement during the climb and descent phases, determined by their respective durations and horizontal speeds. Second, the turnaround time for charging is determined based on the actual arrival and departure times, while the required battery energy for charging is calculated according to the flight distance between the departure and destination airports and the power profile of the corresponding EA during the flight. After each flight,

the batteries of AEA and eVTOL are charged immediately back to 100% SOC upon arriving at the designated parking area. This is necessary to mitigate safety risks associated with maintaining a limited SOC window during flight, such as inadequate power for takeoff or climb, and avoid the unnecessary weight of carrying uncharged batteries. In this article, it is assumed that the initial SOC of each aircraft is 100% at the start of every day and the battery operating temperature is 25°C. Another assumption is that there would be sufficient chargers available to charge each aircraft and that there are no limitations on the airport charging power capacity.

The charging demand is influenced by several key parameters, including the charging duration, required charge energy, and the number of EA. These factors are determined by flight schedule and aircraft size. Therefore, in this section, three case studies are conducted, which examine the impact of large AEA DA-7X, the effect of flight schedules, and the implementation of a simple smart charging strategy. These case studies utilized the 2019 flight schedules from Rotterdam The Hague Airport (RTHA), which provide comprehensive information, including flight number, aircraft registration number, aircraft type, traffic type, arrival and departure airports, and actual times.

### A. Charging Power of Single EA

First, the charging power of individual EA is modeled. In this study, it is assumed that the performance characteristics observed at the cell level would be consistent at the aircraft pack level, provided that appropriate thermal management systems, battery management systems, and operating conditions are maintained. Therefore, the results obtained at the cell level are assumed to be scalable to the aircraft pack level based on the number of cells in the AEA battery pack. As illustrated in Fig. 20,  $P_{ch}$  of various types of AEA and eVTOL with 20% initial SOC and 0.5C C-rate is modeled. In addition,  $P_{ch}$  for the retrofit Cessna 172R at a 1C C-rate is provided. The blue box corresponds to the CC phase of a 1C C-rate, while the gray box represents the CC phase of a 0.5C C-rate. When the charging power reaches its peak value, it transitions from the CC phase to the CV phase. The duration of the CV phase is significant, highlighting the necessity of the ECM model. It can be observed that charging power closely correlates with C-rate and EA battery size. At higher C-rates, the charging time of the retrofit Cessna 172R is shortened. However, the charging power of 1C enters the CV phase earlier because of the higher voltage drop in cell resistance from the higher CC. As a result, the charging time at 1C is not half of that at 0.5C. In addition, the peak charging power for the eight-seater retrofit PC-12 can reach 1 MW, while the small two-seater Pipistrel Velis Electro has insignificant charging power since it has a battery size comparable with an EV.

### B. Case Study of Large AEA DA-7X

The charging demand can be significantly affected by large AEA due to the substantial battery pack size. Therefore, for this case study, the date July 9th is selected, as it includes a flight suitable for replacement by the 16-seater retrofit DA-7X with a 200-km range. The CC–CV charging strategy with a charging rate rated at 0.5C is adopted. If the charging time exceeds the turnaround time required by the flight schedule, the C-rate is increased incrementally by 0.01C steps to satisfy the turnaround time constraints, with a maximum limit of 5C. This C-rate setting also applies to the subsequent case study,

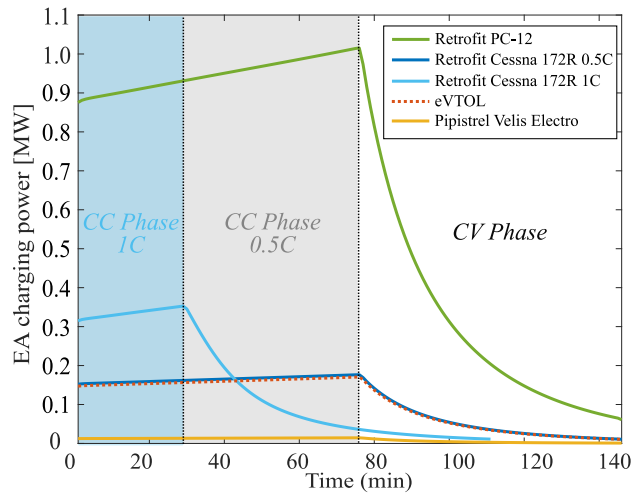


Fig. 20. Charging power of different AEA and eVTOL.

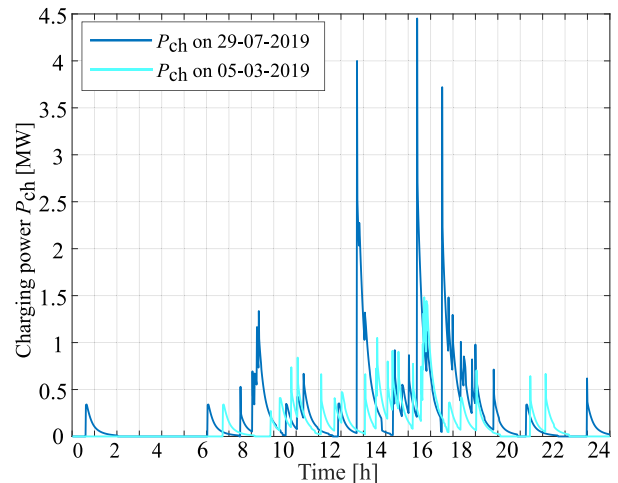


Fig. 22. Charging demand across varied flight schedules.

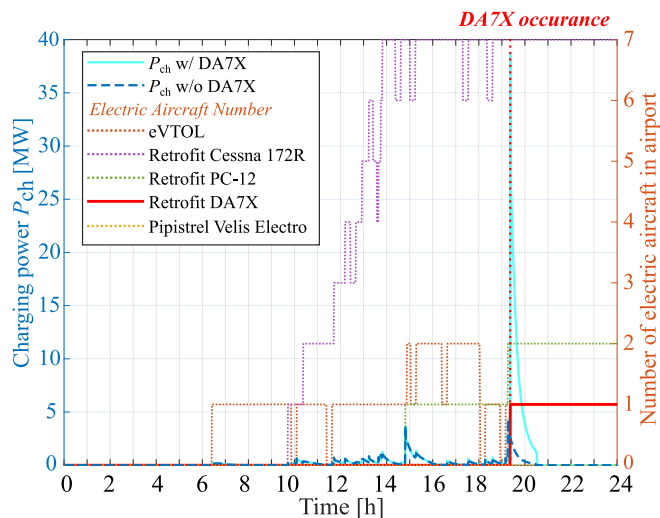


Fig. 21. Charging demand with retrofit DA-7X integration.

excluding the rated C-rate. The charging power profile and the number of EA parked at the airport for the selected date are illustrated in Fig. 21. Two charging power curves are plotted: a light blue solid line considering the retrofit DA-7X, and a dark blue dashed line representing the exclusion of the DA-7X to illustrate its effect. First, distinct peak and off-peak periods are observable within a single day. During off-peak hours, such as in the morning, only small EA, including eVTOL and the retrofit Cessna 172R, are being charged at the airport, with long turnaround times. Prior to the arrival of the retrofit DA-7X, a minor peak power of approximately 4.30 MW is recorded around 19:00, attributed to the landing of the retrofit PC-12, as depicted by the green dotted line. Upon the arrival of the single retrofit DA-7X, a substantial increase in power demand, reaching 38.63 MW, is observed. Despite adopting only a 0.5C charging rate for the retrofit DA-7X, given that there are no subsequent flights scheduled, the charging power remains notably high due to the large battery pack size.

### C. Case Study of Flight Schedule Effects

When examining charging demand from EA, it is essential to acknowledge that this demand is significantly affected by

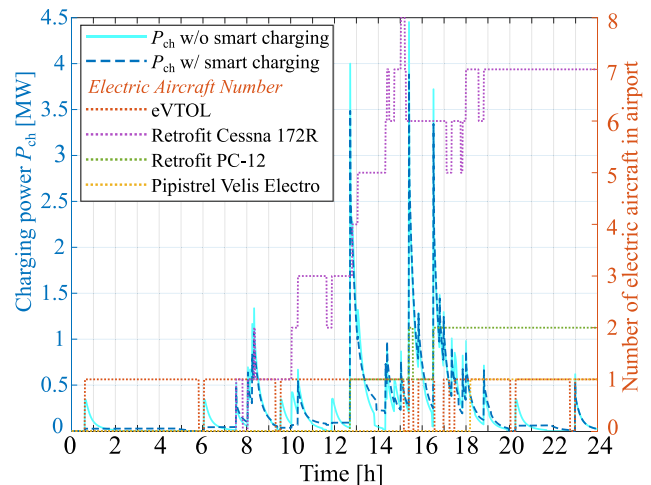


Fig. 23. Charging demand with simple smart charging.

flight schedules, highlighting the need to conduct a case study of flight schedule effects. In this study, two representative cases were specifically selected. The first case, on July 29th, represents one day in the peak summer month of July, which typically experiences high levels of flight activity and increased demand for charging services. The second case, dated March 5th, represents a day in the off-peak month of March, characterized by lower flight demand and reduced charging requirements. In this case study, the charging rate is rated at 1C.

As shown in Fig. 22, the charging demand during the peak summer period at the RTHA can reach up to 4.45 MW during the daytime, indicating a high demand for charging services due to the increased number of flights and short turnaround time between flights. On the other hand, during the off-peak day, the maximum charging power is around 1.48 MW, suggesting a relatively lower demand for charging services. In addition, it is observed that the frequency of charging events is lower during off-peak days compared with peak days. This can be attributed to the reduced flight demand during off-peak periods.

#### D. Case Study of Simple Smart Charging

During extended parking periods, charging at a high C-rate is unnecessary, such as during nights or periods of reduced flight demand. In these scenarios, the implementation of a smart charging strategy is possible, which can effectively manage the charging load, facilitating subsequent grid infrastructure upgrades as needed. In this study, a simple smart charging strategy was adopted on July 29th to investigate the impact of smart charging. Specifically, if there is a subsequent flight, the C-rate is determined by the flight schedule to distribute the charging process throughout the entire turnaround period available. If there is no subsequent flight, the charging is performed at 0.5C.

Fig. 23 shows that implementing a simple smart charging strategy can significantly reduce peak and average power demand. In the original case, the peak power demand reached around 4.45 MW. With the use of simple smart charging, the peak power demand is reduced to approximately 3.88 MW, marking a 13% reduction. When it comes to the average power demand, it decreases from 0.326 to 0.255 kW, representing a reduction of approximately 22%. It is clear from the shown result that the peak load shaving has been effectively achieved via simple smart charging. Hence, if the turnaround time allows, there is no necessity to charge it at high power rates.

#### E. Strategies for Mitigating Peak Power Demand

The large-scale integration of AEA and eVTOL presents challenges to grid capacity and power quality due to its substantial charging power demands. This necessitates the implementation of strategies for mitigating peak power demand. The result in Section VI-B demonstrates that large AEA faces significant challenges, both in demanding requirements for battery energy density and the substantial charging demands. Consequently, an HEA may emerge as a potentially more viable solution for the needs of large aircraft. At the same time, a multifaceted approach is required to address the significant charging power demands of EA. First, adjusting flight schedules can alleviate peak charging demands, a unique feature of EA compared with consumer behavior-oriented EVs. As elaborated in Section VI-C, slight modifications to flight schedules can significantly reduce peak power demand and, consequently, the requirements for grid infrastructure upgrades. Second, implementing a smart charging strategy can optimize charging power profiles. As discussed in Section VI-D, a simple smart charging strategy implementation can reduce the peak power demand significantly. Hence, combining the discussion in Section VI-C, the smart charging strategy for EA can be integrated with flight scheduling. Airport operators can explore scheduling approaches that account not only for aviation considerations but also for other factors such as airport load profiles, renewable energy availability, grid infrastructure capacity, and electricity tariff rates. Last but not least, battery energy storage integration can store excess energy and release it to accommodate higher charging capacities. By employing these strategies, airport operators can manage the high charging power demands of EA more effectively while ensuring grid reliability and optimizing energy utilization.

## VII. CONCLUSION

In conclusion, a preliminary battery sizing method for small, short-range AEA, utilizing a commercial aircraft as a

reference, has been outlined first. This method enables the determination of battery sizes for various AEA based on given top-level design parameters. It establishes an analytical relationship between power profiles across different flight phases, weight components contributing to the takeoff weight, and a set of design constraints. A thorough examination of the takeoff, climb, cruise, descent, and reserve phases is provided. In addition, the methodology considers a detailed AEA powertrain architecture, including the battery pack, dc/dc converter, dc/ac inverter, electric motor, gearbox, and associated cabling, in the calculation of takeoff weight, while integrating the rest of the airframe weight derived from the reference aircraft. Applying this method, three AEA with varying payload capacities are designed, highlighting the escalating need for gravimetric battery energy density as aircraft size increases. For example, the retrofit DA-7X necessitates a 20% increase in energy density compared with the retrofit PC-12. The sizing results also underscore the compromise in range due to the energy density constraint when comparing the retrofit AEA with the reference fuel-based aircraft. As an illustration, the retrofit Cessna 172R can only operate within a range of 250 km, which is only 19.7% of the maximum range of the fuel-based Cessna 172R (1272 km). These results clearly explain the interplay between the range and size of AEA and the battery energy density. Finally, the proposed method is verified using various aircraft and methodologies, ensuring its broad applicability and demonstrating its accuracy.

Estimating the charging power based on the initial CC value in the CC phase is challenging for the CC-CV charging process, as the duration of the CV phase is comparable to that of the CC phase. Hence, to derive the charging power curve, a second-order RC Thévenin-based model is utilized to simulate battery behavior during the CC-CV charging process, accounting for the influence of SOC, C-rate, and temperature on ECM parameters. Building upon battery sizing techniques and the analytical model for the CC-CV charging process, a methodology for accurate charging demand prediction for future AEA and eVTOL is proposed. The proposed model was applied to predict the charging demand of four different AEA types and one eVTOL under a CC-CV charging strategy at RTHA, and various case studies were conducted. The findings of case studies highlight the significant impact of integrating large AEA on the charging demand profile. Incorporating a single retrofit DA-7X leads to a peak charging power nearly ten times that of no integration of the large AEA. Moreover, flight scheduling plays a crucial role as it dictates the charging duration and energy requirements of AEA. In addition, the implementation of simple smart charging techniques effectively reduces peak demand by 13% and average demand by 22% in the case study. This method provides valuable insights for airport operators to anticipate the substantial increase in energy demands resulting from the widespread adoption of EA, which facilitates future flight scheduling for EA and grid infrastructure upgrades. This charging demand prediction methodology can be extended to other aircraft types, airports, and battery technologies. For future research, it is suggested to explore the potential of implementing advanced battery chemistries for AEA, such as LSBs. Furthermore, investigating the integration of larger sized and longer range HEA in future airports is recommended. Smart charging strategies combined with flight scheduling, such as controlling the charging power or scheduling based on local renewable generation or grid congestion, should be

investigated. By doing so, further advancements can be made in optimizing charging infrastructure planning and ensuring sustainable and efficient operations in the era of electrified transportation.

#### ACKNOWLEDGMENT

The contribution of Akshayan Sudharshan of the Department of Electrical Systems and Software, Pipistrel, Ajdovščina, Slovenia, and Jianning Dong of the Department of Electrical Sustainable Energy, TU Delft, Delft, The Netherlands, for their invaluable insights into electric aircraft (EA) battery sizing to this article is gratefully acknowledged. The authors would like to thank Daan van Dijk from Rotterdam The Hague Airport for providing the airport traffic data.

#### REFERENCES

- [1] A. Kasliwal et al., "Role of flying cars in sustainable mobility," *Nature Commun.*, vol. 10, p. 1555, Apr. 2019.
- [2] B. J. Brelje and J. R. Martins, "Electric, hybrid, and turboelectric fixed-wing aircraft: A review of concepts, models, and design approaches," *Prog. Aerosp. Sci.*, vol. 104, pp. 1–19, 2019.
- [3] Y. Liang, G. R. C. Mouli, and P. Bauer, "Charging technology for electric aircraft: State of the art, trends, and challenges," *IEEE Trans. Transport. Electric.*, early access, Nov. 16, 2023, doi: 10.1109/TTE.2023.3333536.
- [4] A. Schwab, A. Thomas, J. Bennett, E. Robertson, and S. Cary, "Electrification of aircraft: Challenges, barriers, and potential impacts," Dept. National Renewable Energy Laboratory, Nat. Renew. Energy Lab., Golden, CO, USA, Tech. Rep. NREL/TP-6A20-80220, 2021. [Online]. Available: <https://www.osti.gov/biblio/1827628>
- [5] C. E. D. Riboldi and F. Gualdoni, "An integrated approach to the preliminary weight sizing of small electric aircraft," *Aerosp. Sci. Technol.*, vol. 58, pp. 134–149, Nov. 2016.
- [6] C. E. D. Riboldi, "An optimal approach to the preliminary design of small hybrid-electric aircraft," *Aerosp. Sci. Technol.*, vol. 81, pp. 14–31, Oct. 2018.
- [7] A. Bills, S. Sripad, W. L. Fredericks, M. Singh, and V. Viswanathan, "Performance metrics required of next-generation batteries to electrify commercial aircraft," *ACS Energy Lett.*, vol. 5, no. 2, pp. 663–668, Feb. 2020.
- [8] I. Geiß and R. Voit-Nitschmann, "Sizing of the energy storage system of hybrid-electric aircraft in general aviation," *CEAS Aeronaut. J.*, vol. 8, no. 1, pp. 53–65, Mar. 2017.
- [9] R. de Vries, M. T. Brown, and R. Vos, "A preliminary sizing method for hybrid-electric aircraft including aero-propulsive interaction effects," in *Proc. Aviation Technol., Integr., Oper. Conf.*, Jun. 2018, p. 4228.
- [10] S. Sun, Q. Yang, and W. Yan, "A novel Markov-based temporal-SoC analysis for characterizing PEV charging demand," *IEEE Trans. Ind. Informat.*, vol. 14, no. 1, pp. 156–166, Jan. 2018.
- [11] K. Qian, C. Zhou, M. Allan, and Y. Yuan, "Modeling of load demand due to EV battery charging in distribution systems," *IEEE Trans. Power Syst.*, vol. 26, no. 2, pp. 802–810, May 2011.
- [12] N. Sadeghianpourhamami, N. Refa, M. Strobbe, and C. Develder, "Quantitative analysis of electric vehicle flexibility: A data-driven approach," *Int. J. Electr. Power Energy Syst.*, vol. 95, pp. 451–462, Feb. 2018.
- [13] Z. Guo, J. Zhang, R. Zhang, and X. Zhang, "Aviation-to-grid flexibility through electric aircraft charging," *IEEE Trans. Ind. Informat.*, vol. 18, no. 11, pp. 8149–8159, Nov. 2022.
- [14] B. Li, Z. Guo, Y. Yuan, and X. Zhang, "Study on the impact of aviation electrification on voltage deviation of the GB transmission system," in *Proc. 57th Int. Universities Power Eng. Conf. (UPEC)*, Aug. 2022, pp. 1–6.
- [15] A. R. Gnadt, R. L. Speth, J. S. Sabnis, and S. R. H. Barrett, "Technical and environmental assessment of all-electric 180-passenger commercial aircraft," *Prog. Aerosp. Sci.*, vol. 105, pp. 1–30, Feb. 2019.
- [16] A. W. Schäfer et al., "Technological, economic and environmental prospects of all-electric aircraft," *Nature Energy*, vol. 4, no. 2, pp. 160–166, 2019.
- [17] M. Mitici, M. Pereira, and F. Oliviero, "Electric flight scheduling with battery-charging and battery-swapping opportunities," *EURO J. Transp. Logistics*, vol. 11, Feb. 2022, Art. no. 100074.
- [18] B. Hou, S. Bose, L. Marla, and K. Haran, "Impact of aviation electrification on airports: Flight scheduling and charging," 2021, *arXiv:2108.08963*.
- [19] J. Cox, T. Harris, K. Krah, J. Morris, X. Li, and S. Cary, "Impacts of regional air mobility and electrified aircraft on airport electricity infrastructure and demand," Nat. Renew. Energy Lab., Golden, CO, USA, Tech. Rep. NREL/TP-5R00-84176, 2023.
- [20] J. Benzaquen, J. He, and B. Mirafzal, "Toward more electric powertrains in aircraft: Technical challenges and advancements," *CES Trans. Electr. Mach. Syst.*, vol. 5, no. 3, pp. 177–193, Sep. 2021.
- [21] D. Raymer, *Aircraft Design: A Conceptual Approach*. Reston, VA, USA: American Institute of Aeronautics and Astronautics, 2012.
- [22] I. Chakraborty, N. S. Miller, and A. A. Mishra, "Sizing and analysis of a tilt-wing aircraft with all-electric and hybrid-electric propulsion systems," in *Proc. AIAA SCITECH Forum*, Jan. 2022, p. 1515.
- [23] G. E. Wroblewski and P. J. Ansell, "Mission analysis and emissions for conventional and hybrid-electric commercial transport aircraft," *J. Aircr.*, vol. 56, no. 3, pp. 1200–1213, May 2019.
- [24] Cessna Aircr. Company. (2011). *Skyhawk Model 172R: Specification & Description*. [Online]. Available: [https://web.archive.org/web/20110511100227/http://textron.vo.llnwd.net/o25/CES/cessna\\_aircraft\\_docs/single\\_engine/skyhawk/skyhawk\\_s%26d.pdf](https://web.archive.org/web/20110511100227/http://textron.vo.llnwd.net/o25/CES/cessna_aircraft_docs/single_engine/skyhawk/skyhawk_s%26d.pdf)
- [25] J. McIver. (2003). *Cessna Skyhawk II / 100—Performance Assessment*. [Online]. Available: <http://www.temporal.com.au/c172.pdf>
- [26] M. Cel, "Cessna 172 flight simulation data," Tech. Rep., 2019.
- [27] X.-G. Yang, T. Liu, S. Ge, E. Rountree, and C.-Y. Wang, "Challenges and key requirements of batteries for electric vertical takeoff and landing aircraft," *Joule*, vol. 5, no. 7, pp. 1644–1659, Jul. 2021.
- [28] T. P. Barrera et al., "Next-generation aviation Li-ion battery technologies—Enabling electrified aircraft," *Electrochem. Soc. Interface*, vol. 31, no. 3, pp. 69–74, Sep. 2022.
- [29] C. E. D. Riboldi, "Energy-optimal off-design power management for hybrid-electric aircraft," *Aerosp. Sci. Technol.*, vol. 95, Dec. 2019, Art. no. 105507.
- [30] J. D. Anderson and M. L. Bowden, *Introduction to Flight Eighth Edition*, vol. 582. New York, NY, USA: McGraw-Hill, 2016.
- [31] P. Sforza, "Refined weight and balance estimate," in *Commercial Airplane Design Principles*, P. Sforza, Ed. Boston, MA, USA: Butterworth-Heinemann, 2014, ch. 8, pp. 301–347.
- [32] MathWorks. (2023). *Electrical Component Analysis: Hybrid and Electric Aircraft*. MATLAB Documentation. [Online]. Available: <https://nl.mathworks.com/help/aeroblks/Electrical-Component-Analysis-Hybrid-and-Electric-Aircraft.html>
- [33] (2020). *Pilot's Operating Handbook Velis Electro. Pipistrel by Textron Aviation*. [Online]. Available: <https://www.domergue.aero/wp-content/uploads/Manuel-de-vol-Pipistrel>
- [34] R. de Vries, R. E. Wolleswinkel, M. Hoogreef, and R. Vos, "A new perspective on battery-electric aviation, part II: Conceptual design of a 90-seater," in *Proc. AIAA SCITECH Forum*, Jan. 2024, p. 1490.
- [35] *U.S. Standard Atmosphere*, NOAA/Nat. Ocean. Atmos. Admin., Washington, DC, USA, 1976.
- [36] W. L. Fredericks, S. Sripad, G. C. Bower, and V. Viswanathan, "Performance metrics required of next-generation batteries to electrify vertical takeoff and landing (VTOL) aircraft," *ACS Energy Lett.*, vol. 3, no. 12, pp. 2989–2994, Dec. 2018.
- [37] L. Patnaik, A. V. J. S. Praneeth, and S. S. Williamson, "A closed-loop constant-temperature constant-voltage charging technique to reduce charge time of lithium-ion batteries," *IEEE Trans. Ind. Electron.*, vol. 66, no. 2, pp. 1059–1067, Feb. 2019.
- [38] A. B. Khan and W. Choi, "Optimal charge pattern for the high-performance multistage constant current charge method for the Li-ion batteries," *IEEE Trans. Energy Convers.*, vol. 33, no. 3, pp. 1132–1140, Sep. 2018.
- [39] K. Li, F. Wei, K. J. Tseng, and B. Soong, "A practical lithium-ion battery model for state of energy and voltage responses prediction incorporating temperature and ageing effects," *IEEE Trans. Ind. Electron.*, vol. 65, no. 8, pp. 6696–6708, Aug. 2018.
- [40] M. Armand et al., "Lithium-ion batteries—Current state of the art and anticipated developments," *J. Power Sources*, vol. 479, Dec. 2020, Art. no. 228708.
- [41] Samsung SDI Co., Ltd. Battery Bus. Division. (2016). *Specification of Product for Lithium-ion Rechargeable Cell: INR18650-35E*. [Online]. Available: <https://datasheet.octopart.com/INR18650-35E-Samsung-datasheet-103126726.pdf>
- [42] L. Lam, P. Bauer, and E. Kelder, "A practical circuit-based model for Li-ion battery cells in electric vehicle applications," in *Proc. IEEE 33rd Int. Telecommun. Energy Conf. (INTELEC)*, Oct. 2011, pp. 1–9.



**Yawen Liang** (Graduate Student Member, IEEE) received the B.Sc. degree in electrical engineering and automation from Sichuan University, Chengdu, China, in 2020, and the M.Sc. degree (cum laude) in electrical power engineering from Delft University of Technology, Delft, The Netherlands, in 2022, where she is currently pursuing the Ph.D. degree in electrical engineering with the DC Systems, Energy Conversion and Storage (DCE&S) Group.

Her research interests include the battery systems and the grid integration of electric aircraft.



**Dávid Bodnár** received the B.Sc. and M.Sc. degrees in electrical engineering from the Technical University of Košice, Košice, Slovakia, in 2019 and 2021, respectively. He graduated with a thesis on the energy consumption prediction of electric midibus.

He was working at Delft University of Technology, Delft, The Netherlands, as a Guest Ph.D. Researcher. He is currently working at the Technical University of Košice, as a Ph.D. Student. His research interests include the areas of battery modeling, energy storage systems, and energy management systems.



**Gautham Ram Chandra Mouli** (Member, IEEE) received the bachelor's degree in electrical engineering from the National Institute of Technology Trichy, Tiruchirappalli, India, in 2011, and the master's degree in electrical engineering and the Ph.D. degree for the development of a solar-powered vehicle-to-grid (V2G) electric vehicle charger from Delft University of Technology (TU Delft), Delft, The Netherlands, in 2013 and 2018, respectively.

From 2017 to 2019, he was a Post-Doctoral Researcher with TU Delft, working on research

topics related to power converters for electric vehicle (EV) charging, smart charging of EVs, and trolley buses. He is currently an Assistant Professor of electric mobility with the Department of Electrical Sustainable Energy, TU Delft. He is involved in many projects at the national and EU level concerning electric mobility such as TULIPS, Drive2X, FLOW, FlexEC, and FLEXInet. He is the Coordinator and a Lecturer for Massive Open Online Course (MOOC) on Electric cars on edX.org with more than 200 000 learners from 175 countries. His current research focuses on EVs, EV charging, batteries, power electronics, and the electrification of heavy-duty vehicles.

Dr. Chandra Mouli was awarded the "Most Significant Innovation in Electric Vehicles" at the IDTechEx Show 2018 and the "Best Tech Idea of 2018" by KIJK for the project. He is currently the Vice-Chair of the IEEE Industrial Electronic Society Benelux Chapter.



**Daniele Ragni** received the master's degree in thermomechanical engineering from the Polytechnic University of Marche, Ancona, Italy, in 2007, and the Ph.D. degree from the Faculty of Aerospace Engineering, TU Delft, Delft, The Netherlands, in 2012.

He joined the Section of Wind Energy, Flow Physics and Technology Department, in 2012. As an Associate Professor in aeroacoustics, he worked on the projects NWO-STWs Thames (2016), IPERMAN (2017), Marie Curie ETN SMART-ANSWER (partner, 2016), and European Project ARTEM (partner, 2016). His background in wind energy and propulsion is engaging him in the extension of particle image velocimetry (PIV)-based pressure reconstruction in wind turbine and aircraft propeller blades for academic and industrial aerodynamics research. Notable developments are the usage of porous open foams for the abatement of aeroacoustic noise scattering by pressure fluctuations and his studies on new serrated devices for wind-turbine noise reduction. He collaborates with many academic institutes and research centers worldwide in the field of experimental fluid mechanics, aeronautics, and aerospace. Author of many scientific publications, he delivered more than five international keynote lectures and organized more than two conferences. He has authored and reviewed several international conferences and journals including *Experiments in Fluids*, *Journal of Fluid Mechanics* (JFM), *Physics of Fluids* (PoF), and among others. His research interests cover the development of experimental aeroacoustics (PIV) and its applications to rotors in low/high speed.



**Pavol Bauer** (Senior Member, IEEE) received the master's degree in electrical engineering from the Technical University of Kosice, Kosice, Slovakia, in 1985, and the Ph.D. degree in power electronics from Delft University of Technology, Delft, The Netherlands, in 1995.

He worked partially at KEMA (DNV GL, Arnhem, The Netherlands) on different projects related to power electronics applications in power systems, from 2002 to 2003. He is currently a Full Professor with the Department of Electrical Sustainable

Energy, Delft University of Technology, Delft, The Netherlands, and the Head of the DC Systems, Energy Conversion and Storage Group. He is also a Professor at Brno University of Technology, Brno, Czech Republic, and an Honorary Professor at The Polytechnic University Timisoara. He published over 180 journals and 450 conference papers in his field (with H-factor Google Scholar 61 and Web of Science 41) and he has authored or co-authored over eight books, holds ten international patents, and organized several tutorials at international conferences. He has worked on many projects for industry concerning wind and wave energy, power electronic applications for power systems, HVdc systems, and projects for smart cities such as PV charging of electric vehicles, PV and storage integration, and contactless charging. His main research interests are power electronics for electric vehicle charging and dc grids and systems.

Dr. Bauer is a former Chairman of the Benelux IEEE Joint Industry Applications Society and the Power Electronics and Power Engineering Society Chapter; the Chairman of the Power Electronics and Motion Control (PEMC) Council; the Chairman of the Benelux IEEE Industrial Electronics Chapter; and a member of the Executive Committee of European Power Electronics Association (EPE) and the International Steering Committee at numerous conferences.